



Highly efficient degradation of azo dye Orange G using laterite soil as catalyst under irradiation of non-thermal plasma

Jean-Baptiste Tarkwa^{a,b}, Elie Acayanka^a, Bo Jiang^{b,c}, Nihal Oturan^b, Georges Y. Kamgang^a, Samuel Laminsi^{a,*}, Mehmet A. Oturan^{b,*}

^a Université de Yaoundé I, Département de Chimie Inorganique, Laboratoire de Chimie Physique et Analytique Appliquée, P.O. Box : 812 Yaoundé, Université de Yaoundé I, Cameroon

^b Université Paris-Est, Laboratoire Géomatériaux et Environnement (EA 4508), UPEM, 77454 Marne-la-Vallée, France

^c School of Environmental and Municipal Engineering, Qingdao University of Technology, Qingdao 266033, PR China

ARTICLE INFO

Keywords:

Laterite soil
Photocatalysis
Gliding arc plasma
Orange G
Mineralization

ABSTRACT

In this study, laterite soil containing various mineral oxides (e.g., Al_2O_3 , Fe_2O_3 and TiO_2), used as an alternative catalyst, was combined with gliding arc plasma treatment for Orange G (OG) degradation in aqueous solution. The results showed that the incorporation of laterite soil (as catalyst) in (OG solution exposed to plasma led to a significant degradation enhancement from 17% for plasma treatment alone to almost 100%. Compared with P25 TiO_2 , Fe_2O_3 , and $\text{TiO}_2/\text{Fe}_2\text{O}_3$ photocatalysts, the decolorization rate of OG can be increased from 56, 68 and 75% respectively to 100% after 60 min laterite-mediated plasma treatment. In the calcinated laterite, Fe_2O_3 was considered not only as TiO_2 sensitizer due to its narrow band-gap but also as the heterogeneous Fenton catalyst. These synergistically enhanced the generation of the reactive species, i.e., $\cdot\text{OH}$, in the gliding arc plasma system and thus process efficiency for OG removal. Under optimized operating conditions, approximately 83% mineralization of OG solution was achieved within 60 min of treatment with the combined process. From the kinetics point of view, OG oxidation fitted with Langmuir–Hinshelwood model with the second-order rate constant (k_p) and adsorption constant (K_a) of 5.74 mg min^{-1} and 0.12 L mg^{-1} , respectively, suggesting that the reaction occurs at the catalyst surface. The catalyst was highly stable even after 5 consecutive cycles.

1. Introduction

In recent decades, increasingly water pollution caused by the presence of organic contaminants has particularly attracted significant attention. In this context, development of more effective and sustainable processes for these organics abatement is required for the preservation of aquatic environment. Facing this environmental issue, interest in applying of electrical plasma technology, as one of the advanced oxidation processes (AOPs), for removing organic contaminants from water has increased significantly, mainly owing to its high environmental compatibility and appreciable treatment performance.

Non-thermal plasma techniques in contact with liquids constitute a rich sources of chemical reactive oxygen species ($\cdot\text{OH}$, O^\cdot , O_3 , H_2O_2), reactive nitrogen species (N^\cdot , NO^\cdot , N_2^\cdot) and physical phenomena like the production of shock waves and UV radiation [1,2]. The performance of this technology for treatment of organic pollutants in water is mainly based on the in-situ generation of hydroxyl radical ($\cdot\text{OH}$), a very

strong oxidizing agent, which is capable to mineralize any organic contaminant, i.e. conversion of organics to CO_2 , H_2O and inorganic ions. In addition, it is well known that relatively stable H_2O_2 derived from the combination of $\cdot\text{OH}$, formed by water ionization with a high-energy electron, is incorporated into the bulk solution by diffusion phenomena. Especially, as reported by several studies, the concentration of H_2O_2 could reach up to 2–4 mM while the concentration of O_3 is significantly lesser ($6 \text{ ppm} \leq [\text{O}_3] \leq 18 \text{ ppm}$) in bulk solution in humid air gliding arc non-thermal plasma system [3–5] because of its low water solubility [6]. In electrical plasma processes, H_2O_2 is a weak oxidant and fails to effectively oxidatively react with various organic contaminants. Fortunately, low H_2O_2 oxidation ability is promoted by the addition of Fe^{2+} ion as catalyst to the acidic solution allowing $\cdot\text{OH}$ generation via homogeneous Fenton reactions [7]. However, the performance of above plasma/Fenton coupled process is limited to the acidic condition ($\text{pH} = 3$) and the loss of the Fe^{2+} catalyst by precipitation under ferric hydroxide in neutral and mildly acidic solution constitutes an issue to get over.

* Corresponding authors.

E-mail addresses: samuellaminsin@gmail.com (S. Laminsi), mehmet.oturan@univ-paris-est.fr (M.A. Oturan).

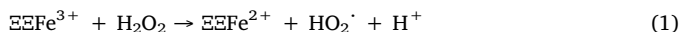
<https://doi.org/10.1016/j.apcatb.2019.01.066>

Received 28 September 2018; Received in revised form 19 December 2018; Accepted 23 January 2019

Available online 24 January 2019

0926-3373/ © 2019 Elsevier B.V. All rights reserved.

To overcome this drawback associated with the Fenton's reaction, the incorporation of natural iron bearing soil or iron (hydr) oxides (e.g., magnetite (Fe_3O_4) or goethite (FeOOH)) have demonstrated as the effective alternatives for catalysis in the combined plasma/Fenton process. These heterogeneous catalysts could improve the degradation efficiency of organic contaminants by $\cdot\text{OH}$ generated from Fenton-like reactions (Eqs. (1) and (2)) [8,9].



On the other hand, many studies [10,11] reported that up to 28% of the input energy was consumed for the generation of UV radiation in electric plasma process [12]. In humid air non-thermal plasma, UV radiation was produced due to the decay of the excited nitrogen molecules [13] and the recombination reaction of some other active species. For instance, Anpilov et al. [14] have reported that the radiation emitted in non-thermal plasma discharge covered a soft UV region ($430 \geq \lambda \geq 190 \text{ nm}$). Moreover, the average emission spectra of gliding arc recorded from 220 to 400 nm using an intensified charge-coupled device (ICCD) based imaging spectrometer, exhibited the intensities of NO, HO and N_2 excited species [15]. Once more, Gharagozalian et al. [16] have reported different ultraviolet peaks at 364.5, 388.5, 388.9 and 397 nm in an emission spectrum of gliding arc air plasma. Non-thermal plasma emitted UV radiation ($\lambda > 185 \text{ nm}$) penetrates into the bulk of an aqueous solution where it can produce photochemical reactions such as organic molecules excitation or semiconductor oxides (e.g. TiO_2 , Fe_2O_3 , etc.) photoactivation [1]. Therefore, UV light could greatly improve $\cdot\text{OH}$ generation through homogeneous and/or heterogeneous photo-Fenton or photocatalysis. Particularly, electrical discharges at atmospheric pressure offer an advantage of eliminating the requirement of artificial UV lamps for aqueous pollutants removal in conventional photocatalysis process.

Now, to promote the energy efficiency of electric plasma process, several studies involving the combined non-thermal plasma and photocatalysis process have been carried out for the effective degradation of organic contaminants in aqueous phase [17,18]. For instance, $\text{TiO}_2(\text{P25})$ photocatalyst was applied in a plasma discharge system to use ultraviolet radiation from discharge and exhibited higher organic contaminants removal efficiency and energy efficiency [19,20]. However, TiO_2 photocatalyst has relatively high band gap energy, approximately 3.2 eV and thus can be only activated by UV light ($\lambda < 387 \text{ nm}$). Moreover, the performance of TiO_2 photocatalyst is inherently limited by the recombination of photo-generated charges carriers as it reduces the quantum efficiency of the global photocatalytic process [21,22]. Consequently, the discharge energy of plasma cannot be used efficiently in TiO_2 plasma-photocatalysis. But, in combination with co-catalyst such as Fe^{3+} or in heterojunction hybrid with other semi-conductors, TiO_2 plasma-photocatalysis is reported efficient in plasma energy consumption [23]. In light of this, naturally heterogeneous iron/titania bearing catalysts can be used for economical and practical reasons.

Laterite soil is one of the important and novel catalysts, which is abundant in some parts of the earth including Africa [24]. It is found that laterite is essentially a mixture of ferric hydroxide, aluminum hydroxide, titanium, rarely manganese and free silica in varying proportions [25]. Thus, recently, many studies were dedicated to the utilization of laterite as the heterogeneous catalyst in Fenton-like reactions [24,26]. However, till now, few literature paid attention to the combined electric plasma/afterite process for aqueous contaminant removal and thus no information involving the comprehensive role of laterite in plasma system is available. Therefore, the present work is devoted to investigate a natural laterite ($x\text{Al}_2\text{O}_3$, $y\text{Fe}_2\text{O}_3$, $z_1\text{SiO}_2$, $z_2\text{TiO}_2$) soil as catalyst in combination with non-thermal plasma treatment for the oxidative degradation of OG aqueous solution. This purpose is to demonstrate whether a natural laterite soil is able to act as a catalyst and/

or photocatalyst under gliding arc non thermal plasma irradiation to degrade the azo dye OG and to evaluate the effect of the operating conditions on the decolorization rate.

2. Experimental

2.1. Materials and chemicals

Analytical grade chemicals were used without further purification. The azo dye OG ($\text{C}_{16}\text{H}_{10}\text{N}_2\text{Na}_2\text{O}_7\text{S}_2$, $\lambda_{\text{max}} = 478 \text{ nm}$ and $\text{Mw} = 452.36 \text{ g mol}^{-1}$) was purchased from Sigma-Aldrich. Reagent quality Na_2CO_3 and NaHCO_3 were used for preparation of ionic chromatography mobile phase. Sulfuric acid, ammonium acetate, and methanol used for liquid chromatography analyses were HPLC grade from Sigma-Aldrich. Pure Fe_2O_3 and $\text{TiO}_2\text{-P25}$ Degussa were purchased from sigma Aldrich and were used for control experiments, using equivalent contained amounts in 3 g L^{-1} of natural laterite soil. Special kits (spectroquant® test kit reagent Fe-1) of analytical grade were purchased from Merck Germany and were used for leaching iron measurement. The natural laterite soil was collected from Adamaoua region, Cameroon. Then, it is crushed to obtain a powder and used without any further treatment after calcination.

2.2. Characterization

The chemical composition of the natural laterite soil was determined using atomic absorption spectrophotometer (Varian 220Z furnace model). Once collected from the site, the laterite was grounded into powder with the average particle diameter of $200 \mu\text{m}$ before chemical composition analysis. The crystal structure was analysed by X-ray diffraction (XRD) of the samples, performed on a Siemens D5000 diffractometer using the $\text{K}\alpha$ radiation of Cu ($\lambda = 1.5418 \text{ \AA}$). The ICDD-JCPDS (International Centre for Diffraction Data - Joint Committee on Powder Diffraction Standards) database was used to identify the crystalline phases. The Raman spectrum of catalyst was recorded using Renishaw InVia Raman Spectrometer equipped with 532 nm NDYAG Laser. The functional groups of crude and heated laterite were detected by Fourier Transform Infrared spectroscopy (FTIR, Nexus 670, Thermo Nicolet, Germany). The specific BET surface area and pore size distribution were determined using N_2 adsorption-desorption experiments (Micromeritics ASAP2020). The laterite sample was calcined in an air atmosphere furnace pre-set at constant temperature.

2.3. Experimental set-up and treatment procedure

All experiments were carried out in a 500 mL gliding arc plasma reactor [27]. The experimental system in Fig. 1 was initiated by a high voltage generator (an Aupem Sefli HV transformer: 10 kV; 160 mA in open conditions), which produce an electric arc between two diverging knife-shaped electrodes. The ignited electric arc was blown along the electrodes axis like plumes by a jet of wet air coming from an air compressor and humidified in a bubbler containing distilled water. The plasma plume was in contact with the aqueous solution so that the reactive primary species could react with substrates in the interface between liquid and gas phases or diffuse into bulk solution to generate daughter reactive species. After the decay of the plasma plumes, the evolution repeats from the initial break-down between two diverging electrodes. The specific energy input (SEI) in the discharge is defined as follow (Eq. (3)) [6] :

$$\text{SEI}(\text{kWh m}^{-3}) = \frac{\text{disch arg epower (kW)}}{\text{gasflowrate}(\text{m}^3 \cdot \text{h}^{-1})} \quad (3)$$

Under the experimental conditions listed in Table 1, the specific energy input was estimated between 0.21 and 0.26 kWh m^{-3} for a controlling high voltage ranging from 7 to 10 kV.

Before it was used, the grounded laterite soil was calcined at an

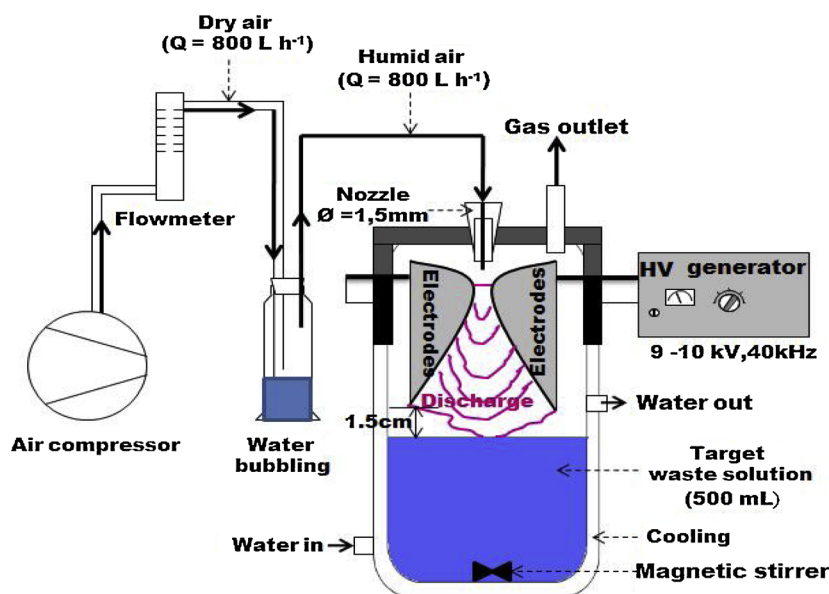


Fig. 1. Glidarc experimental device.

Table 1
Experimental conditions.

Parameters	Values
Applied voltage (kV)	10
Power frequency (Hz)	50
Electrode material	Stainless steel
Electrode thickness (mm)	3
Minimum electrode gap (mm)	2.5
Gas type	Humid air
Gas flow rate (L h ⁻¹)	800
Relative humidity (%)	55 ± 5

appropriate temperature (400 or 800 °C) for 3 h. For reuse, the used catalyst was recovered after each cycle, washed with distilled water and dried for 6 h at 105 °C in an oven. For each treatment, 500 mL of OG solution was used and the pH was adjusted to an appropriate value (3–10). An aqueous suspension of the laterite was prepared by adding a suitable quantity of catalyst into OG solution. After 20 min of adsorption under dark, the gliding arc reactor system was filled with the suspension and placed under magnetic stirring. All experimental parameters for gliding arc system were set as listed in Table 1. The aqueous mixture was exposed to the discharge for different times ranging from 0 to 60 min. Aqueous samples were withdrawn at fixed interval time and centrifuged at 6000 rpm for 10 min. The filtrate was then analyzed.

2.4. Analytical methods

The dye concentration of OG was determined by measuring the absorbance of the solution at maximum wavelength ($\lambda_{\max} = 478$ nm) using a DR3900 spectrophotometer. The decolorization efficiency of OG was determined according to Eq. (4):

$$\text{Decolorization efficiency} = \frac{C_0 - C_t}{C_0} \times 100 \quad (4)$$

where C_0 is the initial concentration of OG and C_t is the remained concentration at time t .

The pH of the OG solution was measured with a Hanna HI 9811-5 electronic multi meter. The concentration of released SO_4^{2-} was determined with a Dionex AS4A-SC, 25 cm x 4 mm (i.d.) anion-exchange column using a mixture of 1.8 mM Na_2CO_3 and 1.7 mM NaHCO_3 solution at 2.0 mL min⁻¹ as mobile phase. The residual total organic carbon (TOC) of treated solutions was monitored with a Shimadzu TOC

analyzer VCSH with ± 2% accuracy using the non-purgeable organic carbon method. The leached iron was spectrophotometrically monitored using a spectroquant® iron test kit "reagent Fe-1" at a maximum wavelength of 436 nm.

3. Results and discussion

3.1. Characterization of the catalyst "laterite"

The chemical compositions of non-heated and calcined laterite soil were given in Table 2.

As shown in Table 2, three oxides, i.e., Al_2O_3 , Fe_2O_3 and TiO_2 are the major constituents in the crude and calcined laterite samples. The contents of MnO, MgO, CaO, Na_2O and K_2O are lower than the limit of detection of 0.01%. Although exhibiting no photocatalytic activity, alumina was reported as a good catalyst support in wastewater treatment [28]. In addition, TiO_2 was the most commonly used semiconductor photocatalyst owing to its high efficiency and stability. While iron oxides possess narrow band gap energy and thus were considered as a good visible light photocatalyst [29]. Accordingly, this laterite soil is reasonably expected to be an excellent natural catalyst and/or photocatalyst. Fig. 2 demonstrates the XRD peaks of non-calcined and calcined laterite catalyst. The XRD pattern of non-heated laterite (Fig. 2(a)) reveals the presence of several mineral oxides in accordance with chemical analysis (Table 2). In all the spectra, the peaks at 2θ values of 25.32°, 36.90°, 47.98°, 55.00° and 62.70° can be attributed to (103), (200), (105), (204) and (116) space planes of anatase, respectively (JCPDS 83–2243). The diffraction peaks at 2θ values of 24.20°, 33.14°, 35.50°, 40.90°, 54.10°, and 64.00° are characteristics of (012), (104), (110), (113), (116) and (300) plane of hematite crystal structure, respectively. Moreover, in the spectrum of non-heated laterite, the peaks at 2θ values of 49.60° and 57.90° can be assigned respectively to (024) and (018) space plane of hematite (JCPDS 33-0664). From

Table 2
Chemical analysis of the non-heated and 400 °C heated laterite soils.

Samples	Al_2O_3	Fe_2O_3	TiO_2	SiO_2	P_2O_5	LOI*	Total
Non-heated (%)	50.38	15.08	3.65	0.75	0.18	28.61	98.66
400 °C heated (%)	71.46	21.39	5.17	1.06	0.25	/	99.34

* LOI: Loss on Ignition.

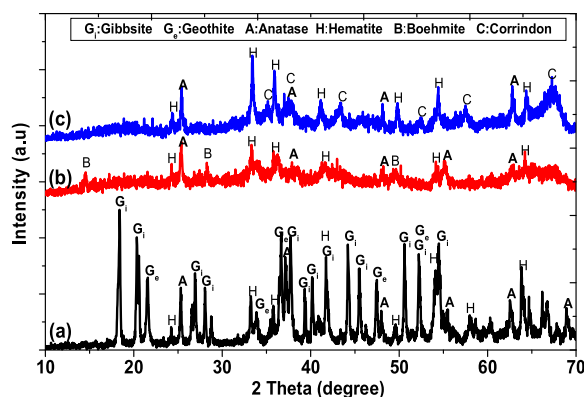


Fig. 2. XRD patterns of: (a) uncalcined laterite, (b) calcined laterite at 400 °C and (c) calcined laterite at 800 °C.

Fig. 2(a), the diffraction peaks at 2θ values of 21.40°, 33.20°, 36.70°, 47.40° and 54.22° are ascribed to (110), (130), (111), (041) and (240) plane of goethite, respectively (JCPDS 29-0713). These peaks disappear upon calcination due to goethite dehydration into hematite (Fig. 2(b)). The XRD peaks at 2θ values of 18.38°, 20.32°, 26.90°, 28.04°, 37.70°, 39.32°, 40.10°, 41.72°, 44.20°, 45.46°, 50.60°, 52.22°, and 54.40° in non-heated laterite correspond to (002), (110), (11-2), (112), (311), (31-2), (022), (312), (-313), (023), (32-2), (024) and (314) plane of gibbsite phase, respectively (JCPDS 33-0018). Upon calcination at 400 °C, these peaks disappear, suggesting the dehydroxylation of gibbsite. This transformation can be evidenced by the appearance of new peaks in Fig. 2(b) at 14.56°, 28.26°, 49.32° and 64.2°, which correspond to (020), (120), (200) and (231) spacing planes of boehmite, respectively (JCPDS 21-1307). Furthermore, at 800 °C the boehmite characteristic peaks disappear with the formation of the other new peaks in Fig. 2(c) at 2θ values of 35.16°, 37.80°, 43.42°, 52.56°, 57.50° and 66.50° which can be assigned, respectively, to (104), (110), (113), (024), (116) and (214) spacing planes of α -Al₂O₃ (JCPDS 42-1468). As reported by Al-Sheeha et al. [30], boehmite was dehydrated by heating and transformed to the most stable α -Al₂O₃ phase through the successive transformation of the metastable alumina phases, i.e., γ -, δ -, θ -Al₂O₃.

Fig. 3 depicts the Raman spectroscopy of laterite calcined at 400 °C. The peaks at 226, 293, 411 and 1326 cm⁻¹ are characteristic of hematite vibration mode [31]. It was reported that anatase TiO₂ owns six Raman active mode: 2B_{1g} (399 and 520 cm⁻¹), 3E_g (144, 197 and 639 cm⁻¹) and A_{1g} (513 cm⁻¹) [32]. Thus, peaks at 145 and 520 cm⁻¹ are characteristics of TiO₂ anatase phase. Finally, the peaks at 352 and 678 cm⁻¹ can be assigned to boehmite phase.

Fig. 4 depicts FTIR spectra of uncalcined and calcined laterite soils. In uncalcined laterite spectrum, the peak at 3620 cm⁻¹ is characteristic

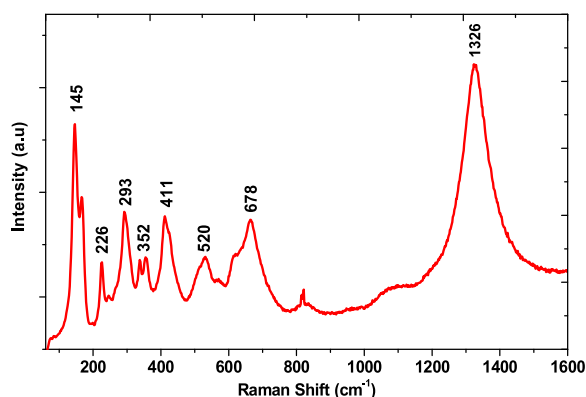


Fig. 3. Raman spectrum of calcined laterite at 400 °C.

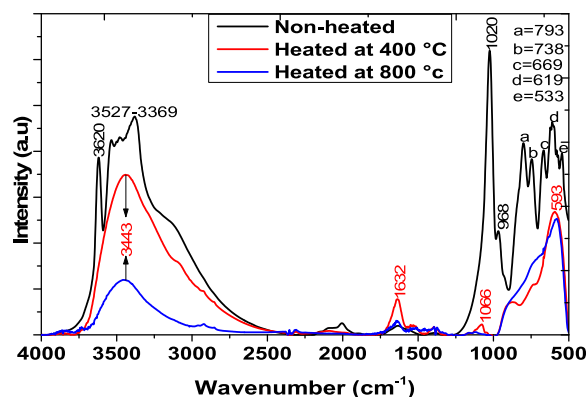


Fig. 4. FTIR spectra of uncalcined laterite and that of samples calcined at 400 °C and 800 °C.

of inner OH groups stretching vibration, whereas the broad band at 3527–3375 cm⁻¹ is due to OH stretching vibration modes of gibbsite and goethite [33]. The peaks at 669, 968 and 1020 cm⁻¹ are assigned to gibbsite OH groups bending mode [34]. The peaks observed at 738 and 533 cm⁻¹ are separately attributed to the stretching vibration of Fe–O and Fe–O–H [35]. Moreover, the peaks at 793 and 619 cm⁻¹ are associated to translation and the deformation bands of goethite OH groups [36]. The FTIR spectra patterns of heated laterite samples presented a broad band at 3442 cm⁻¹, which is characteristic of O–H stretching vibration. Upon calcination, this band becomes weakened in intensity from 400 °C to 800 °C of calcination due to the dehydration at high temperature. The spectrum of laterite heated at 400 °C presents a characteristic vibration peak of hematite at 1632 cm⁻¹, which is observed during thermal transformation between goethite and hematite [37]. The band appearing at 1066 cm⁻¹ is due to Al–OH bending vibration of boehmite, arising from gibbsite dehydroxylation at 400 °C. Meanwhile, the disappearance of this peak at 800 °C confirms the dehydration of boehmite into alumina. Literature has reported a steady decrease in intensity of boehmite peak at 1066 cm⁻¹ with increasing temperature up to 450 °C and then a large decrease as a result of further increasing calcination temperature above 450 °C [38]. In addition, the band appeared between 500 and 700 cm⁻¹ is associated to Ti–O–Ti vibrations of TiO₂ [19].

According to IUPAC classification the BET isotherms in Fig. 5(a) are type IV, suggesting mesoporous materials. Moreover, Fig. 5(b) displays the pore-size distribution with mesoporous (2–50 nm) particles. The low specific surface area of crude laterite is due probably to the presence of impurities embedded in the pores of metal oxides and hydroxides. However, when being calcined at 400 °C, these impurities can be pyrolyzed or volatilized, resulting in the much more appearance of voids. Hence a high surface area is observed for calcined laterite compared to non-heated sample. Especially, laterite calcined at 400 °C presented a very large specific area due to the presence of boehmite (AlOOH) because of its lamellar structure. For instance, Mendoza-Damián et al. [28] has reported a specific area of 213 m² g⁻¹ for boehmite and high adsorption capacity for phenol molecules. In addition, at this temperature, both TiO₂ and Fe₂O₃ are well crystallized, exhibiting high dispersion levels in the alumina support. But, by heating the crude laterite at 800 °C, the particles size decreases due to the aggregations. As the calcination temperature increases, crystallites tend to agglomerate, which generates bigger crystal particles and therefore results in the decrease in the surface area.

3.2. Catalytic activity tests of laterite in gliding arc plasma reactor

3.2.1. Operating parameters

The calcination temperature of catalyst is an important parameter which affects the nature of the crystalline phases, their crystallinity and

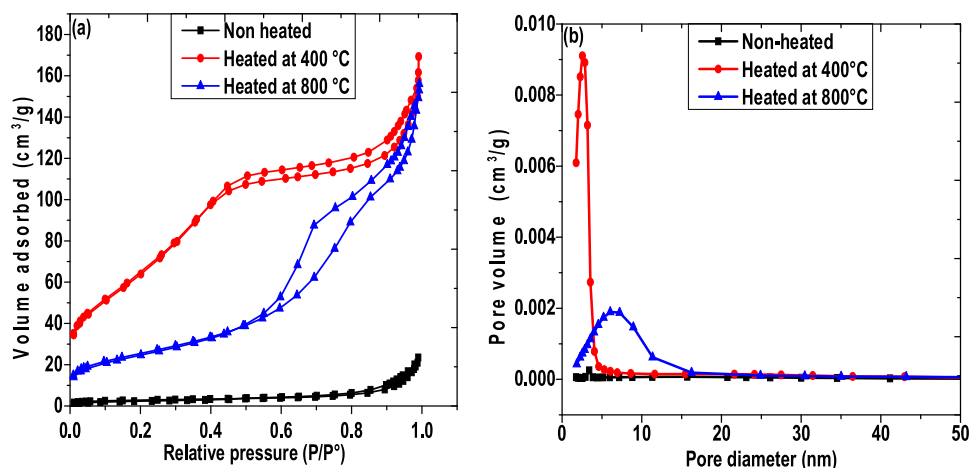


Fig. 5. (a) Nitrogen sorption isotherms and (b) Pore-size distribution of samples.

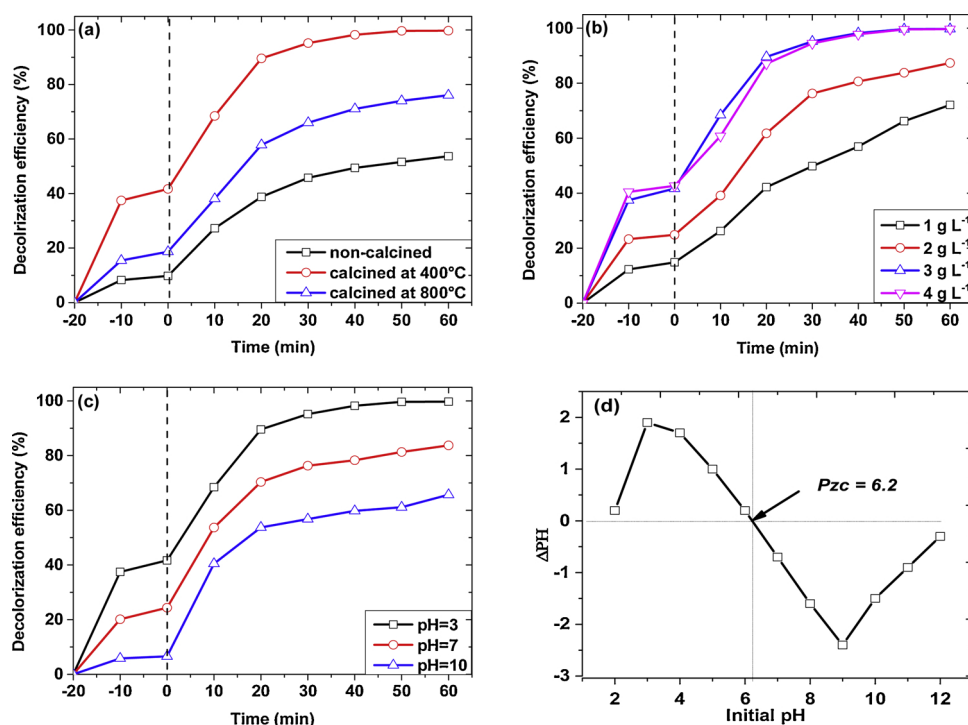


Fig. 6. Effects of key operating parameters on decolorization efficiency of 0.1 mM OG solution in gliding arc plasma treatment : (a): calcination temperature ($\text{pH} = 3$, 3 g L^{-1} of laterite); (b): Catalyst load ($\text{pH} = 3$); (c): Initial pH (3 g L^{-1} of laterite); (d): Point of zero charge of 400 °C heated laterite.

Table 3

Textural properties of non-heated and calcined laterite samples.

Samples	Non-heated	Heated at 400 °C	Heated at 800 °C
Total surface area ($\text{m}^2 \text{g}^{-1}$)	9.59	253.13	90.60
Total pore volume ($\text{cm}^3 \text{g}^{-1}$)	0.03	0.24	0.23
Average pore diameter (nm)	13.70	4.00	7.39

the particle sizes; hence it may affect the process efficiency. Fig. 6(a) shows the effect of calcination temperature on the plasma-catalytic decolorization of OG. It can be seen that the decolorization efficiency recorded after 60 min of treatment was 55% with non-heated laterite, while for the 400 °C and 800 °C calcined laterite, 100% and 76% of OG decolorization were obtained, respectively. In the case of non-heated laterite, many catalytic sites were probably masked by surface impurities. But during the calcination process, the impurities were eliminated and meanwhile laterite became more crystalline. These

suggestions can be validated by the results of XRD and FTIR analysis given above. As a result, calcination treatment would endow the laterite with much more active sites exposure to the plasma, facilitating the oxidative degradation of OG. This may be the reasons for the superior performance of plasma system mediated by calcinated laterite over that of the counterpart system with non-heated laterite. But too high calcination temperature induces the agglomeration of small particles. Consequently, laterite calcined at 800 °C had inferior surface area to that calcined at 400 °C (Table 2). Thus, further increasing the calcination temperature from 400 °C to 800 °C decreased the number of active sites on the surface of laterite and therefore the performance for OG degradation. Considering the results of Fig. 6(a), the catalyst calcined at 400 °C was used to optimize the OG oxidation (Table 3).

Fig. 6(b) depicts the effect of laterite load on OG decolorization efficiency in the combined plasma-catalytic process. Increasing the catalyst load from 1 to 3 g L^{-1} improved OG decolorization from 74 to 100% within 60 min treatment. As the catalyst load increased, more

active sites were available and better adsorption of dye was obtained. However, when higher load of laterite catalyst was applied, more photo-generated charge carriers could be formed and more $\cdot\text{OH}$ s were generated from H_2O_2 decomposition with surface iron species. Thus, increasing catalyst load facilitated the photo-generation of the holes and thereby $\cdot\text{OH}$. Nevertheless, no improvement, but a slight decrease on OG decolorization efficiency was observed by the catalyst dose increasing to 4 g L^{-1} . Overall, the increase of catalyst load could result in an increase of the solution turbidity and thus could hinder the UV light penetration, which therefore lessened the production of reactive species due to insufficient photo-activation of catalyst. This fact was also reported by some research teams explaining the decrease of the UV light penetration as a consequence of the solution turbidity caused by the small particle size of photocatalyst [39,40]. Accordingly, the optimal catalyst load for OG decolorization under gliding arc plasma discharge can be considered as 3 g L^{-1} .

The effect of initial pH on the process efficiency was depicted in Fig. 6(c). It can be observed that the decrease of pH from 10 to 3 led to the increase of OG decolorization rate from 71% to almost complete decolorization (100%), within 60 min of treatment. This result shows that the acidic pH was more favourable for OG decolorization due partly to the enhancement of Fenton-like reaction (Eqs. (1) and (2)), which is optimal at pH 3. In addition, as shown in Fig. 6(d), the catalyst point of zero charge (pzc) was founded to be 6.2. Thus, laterite surface was positively charged at lower pH values, which was favourable for the adsorption of OG anionic dye over the laterite via electrostatic attraction. In light of this, with 3 g L^{-1} of lateritic soil, 40% of OG was degraded at pH 3 while only 7% was removed at pH 10 within 20 min of treatment time (Fig. 6(c)). The complete decolorization of OG solution was then reached at 60 at pH 3. Moreover, in acidic medium the plasma generated H_2O_2 was preferably adsorbed onto catalyst surface while it was decomposed into oxygen and water in alkaline medium [41]. As laterite catalyst was expected to content Fe^{3+} at its surface, once H_2O_2 was plasma generated, Fenton related process (Fenton like or photo-Fenton) could be developed.

3.2.2. Kinetics of the heterogeneous combined process

Several studies in literature reported on the initial rate of Langmuir Hinshelwood kinetics for organic contaminants oxidation with adsorption/desorption equilibrium [42,43]. This model is described by Eq. (5), and gives the relationship between the initial oxidation rate (r) and the initial OG concentration model [44].

$$r = -\frac{d[\text{OG}]}{dt} = k_r \frac{K_s [\text{OG}]}{1 + K_s [\text{OG}]_0} = k_{app} [\text{OG}] \quad (5)$$

From which one can obtain a linear form (Eq. (6)):

$$\frac{1}{k_{app}} = \frac{1}{k_r K_s} + \frac{[\text{OG}]_0}{k_r} \quad (6)$$

where, K_s (mM^{-1}) and k_r (mM min^{-1}) are the adsorption equilibrium constant and the second order kinetic rate constant of surface reaction, respectively.

To obtain the apparent rate constants of Eq. (6), a set of experiments were performed using different initial OG concentration ranging from 0.05 to 0.15 mM at pH = 3 and with catalyst dosage of 3 g L^{-1} . From Fig. 7(a), 99%, 98%, 95% and 86% of decolorization efficiency were achieved after 30 min of treatment for 0.05, 0.075, 0.1 and 0.15 mM OG, respectively. As the dye concentration increased, the ratio of oxidizing species/dye molecules decreased, causing a slower oxidation. The insert plot of Fig. 7(a) displays a pseudo-first-order model of decolorization with a decrease of the apparent rate from 0.186 to 0.076 min^{-1} when increasing initial OG concentration from 0.05 to 0.15 mM, respectively.

A plot of $1/k_{app}$ versus $[\text{OG}]_0$, (Fig. 7(b)) shows that Eq. (6) is well fitted with a regression coefficient of 0.996. From the slope ($1/k_r$) and intercept ($1/k_r K_s$) of this plot, the second order rate constant (k_r) and adsorption constant (K_s) were calculated as $12.70 \times 10^{-3}\text{ mM min}^{-1}$ and 52.71 mM^{-1} , respectively. These results show that adsorption was the controlling step in the whole laterite-mediated plasma-catalysis process. Similar observation was also made by Sun et al. [45] showing that OG degradation using nanosized $\text{Sn(IV)/TiO}_2/\text{AC}$ photocatalyst at pH 2 is fitted by Langmuir-Hinshelwood kinetic model.

3.2.3. Stability of catalytic performance of the laterite

Recovery and reuse of the catalyst are the economically important aspects in the application for wastewater treatment. With the purpose to evaluate the laterite catalyst stability, recycle experiments were performed for six cycles with the same sample and experimental conditions. The performance of the catalyst for 6 cycles of consecutive use is shown in Fig. 8(a). These results indicate a slight decrease in catalytic efficiency after the first cycle. However, for the 2nd and 3rd cycle the effectiveness were the same. The decolorization efficiency of 99%, 93%, 90%, 90%, 88% and 83% were obtained on 1st, 2nd, 3rd, 4th, 5th and 6th cycles, respectively, after 60 min of treatment. Nonetheless, 12% of efficiency loss was recorded after five cycles reflecting a slight deactivation or leaching phenomena of catalyst during the treatment.

Under the working conditions (pH = 3), the acidic TiO_2 semiconductor ($\text{pH}_{pzc} = 6.5$) is known to be stable while amphoteric hematite oxide may undergo a photo-dissolution process [46]. Fig. 8(b) depicts the leached iron concentration during the treatment. The results show that, the percentage of dissolved iron ions after 60 min was limited ($< 0.2\%$ of initial loading), indicating the remarkable stability of $\alpha\text{-Fe}_2\text{O}_3$ during the process. As already reported by Zhang et al. [36], the $\alpha\text{-Fe}_2\text{O}_3$ dissolution process was delayed by the presence of the natural boehmite support. In addition, a similar observation was also made by Li et al. [47] that the $\text{Fe}_2\text{O}_3/\text{AlOOH}$ system remained relatively stable after 6 cycles due to the positive surface charged of alumina AlOOH ($\text{pH}_{pzc} = 7.5$), which inhibited iron oxide dissolution and/or facilitated the feedback of dissolved iron species onto iron oxide. Once more, the large number of plasma generated and photo-excited electrons can enhance surface Fe^{3+} reduction and therefore improve the cycle reaction efficiency of surface attached $\text{Fe}^{3+}/\text{Fe}^{2+}$. Hence, less Fe^{3+} ions should be dissolved from the laterite into the solution.

3.3. Mineralisation of OG aqueous solution with the combined process

Under optimal decolorization conditions, experiments were performed in order to achieve OG mineralization by following the TOC removal and the concentration of the released sulphates ions during the degradation. As can be seen in Fig. 9, complete degradation of OG and 83% TOC removal was achieved within 60 min of treatment. Moreover, the mineralization process released about 0.2 mM of sulphates ions, which correspond to the concentration in OG before treatment. This constitutes another evidence of mineralization of OG solution. Therefore, upon covalent bond cleavage in OG molecules and oxidation of the resulting lower molecular weight species, the SO_3^- groups were released and recovered as SO_4^{2-} .

3.4. Synergetic effect of plasma and laterite on decolorization of OG solution

To investigate the synergetic contribution of different processes which may occur in plasma/laterite-photocatalysis process during OG oxidation, four parallel experiments including plasma alone, plasma/ TiO_2 , plasma/ Fe_2O_3 and plasma/laterite were performed and results are presented in Fig. 10. For these experiments, TiO_2 and Fe_2O_3 load

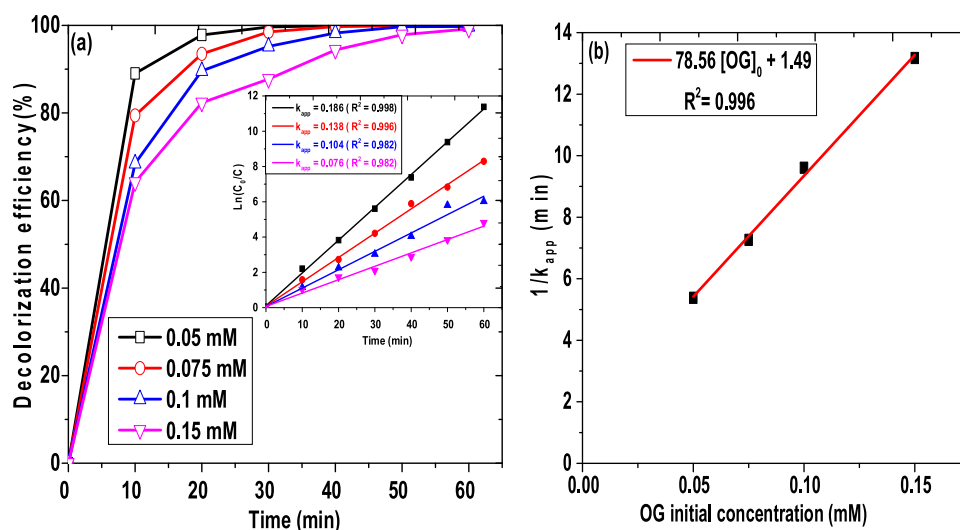


Fig. 7. Effect of initial OG concentration on the decolorization efficiency (a) and relationship between $1/k_{app}$ and initial OG concentration (b) at following operating conditions: Laterite concentration: 3 g L^{-1} and $\text{pH} = 3$. The insert of Fig. (a) displays apparent pseudo-first-order reaction kinetics.

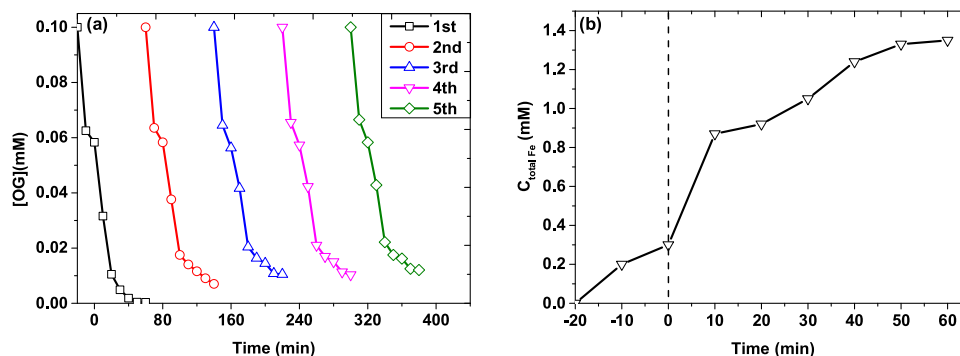


Fig. 8. (a) Stability of laterite (catalyst) after 5 consecutive cycles (a) and total iron ion release during the 1st cycle treatment (b).

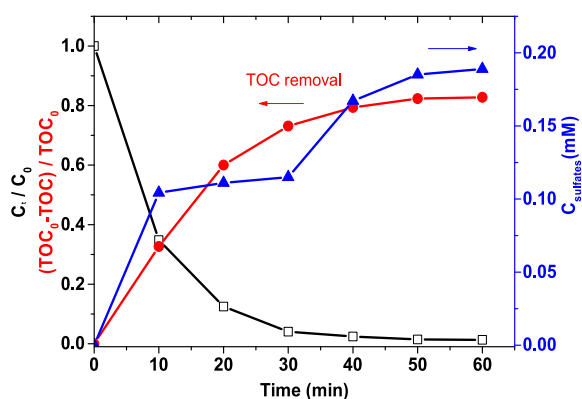


Fig. 9. Degradation (□) and mineralization (●) performance and evolution of sulfate ion concentration (▲) under gliding arc plasma treatment using Laterite catalyst. $[OG] = 0.1 \text{ mM}$, $\text{pH} = 3$, $[laterite] = 3$; 3 g L^{-1} .

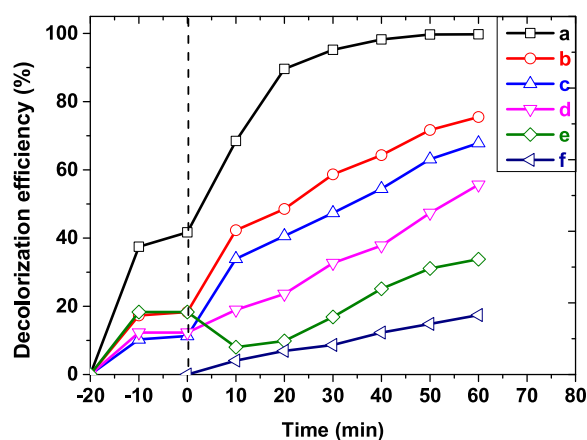


Fig. 10. Decolorization efficiency of 0.1 mM OG aqueous solution ($\text{pH} = 3$) in different experimental conditions: (a): plasma + laterite (3 g L^{-1}), (b): plasma + TiO_2 (0.16 g L^{-1}) + Fe_2O_3 (0.64 g L^{-1}), (c): plasma + Fe_2O_3 (0.64 g L^{-1}), (d): plasma + TiO_2 (0.16 g L^{-1}), (e): plasma + laterite (3 g L^{-1}) + t -butanol (30 mL L^{-1}), (f): plasma alone.

were used according to their equivalent contents in 400°C calcined laterite. It can be observed that 17% of decolorization efficiency was obtained after 60 min with gliding arc alone (Fig. 10(f)). However, the incorporation of laterite to gliding arc reactor system improved the decolorization efficiency (Fig. 10(a)), with almost complete decolorization at 60 min of treatment. As illustrated in Fig. 10(d), plasma- TiO_2 photocatalysis at 0.16 g L^{-1} of TiO_2 resulted in 55% decolorization

efficiency at 60 min treatment, indicating a remarkable improvement of efficiency despite the low load of TiO_2 . As reported by Acayanka et al. [17], this enhancement may be due to additional $\cdot\text{OH}$ formation from TiO_2 photocatalysis under plasma irradiation. On the other hand, with

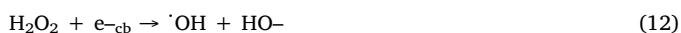
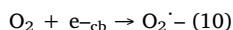
0.64 g L⁻¹ of Fe₂O₃ (Fig. 10(c)), 68% of decolorization was achieved. This positive result could be explained by catalytic contribution of Fe₂O₃, based on the following aspects. When added Fe₂O₃ in gliding arc system, more $\cdot\text{OH}$ could be generated from H₂O₂ decomposition through Fenton-like reactions (Eqs. (1) and (2)) and Fe₂O₃ photocatalysis. Moreover, when both Fe₂O₃ and TiO₂ were used, 75% of decolorization was obtained, indicating a slight increase with TiO₂-Fe₂O₃ heterojunction. Nevertheless, TiO₂-Fe₂O₃ system, allowed 75% of OG decolorization while almost complete decolorization was achieved with laterite calcined at 400 °C. Therefore, boehmite has played an important role according to the following aspects. Its reported that high specific area [48] was favourable to well dispersion of TiO₂ and Fe₂O₃ and also OG adsorption through its active Lewis sites. Moreover, although boehmite was considered as dielectric material, it could exhibit photocatalytic properties due to the presence of surface defects (anion vacancies) [49]. However, upon absorption of photons, the defects can photogenerated electron with sufficient energy to O₂ reduction while the holes can react with HO- to generate additional $\cdot\text{OH}$ for OG oxidation. In order to reveal the role of reactive species, an experiment was performed with *t*-butanol as a scavenger to investigate the role of $\cdot\text{OH}$. As shown in Fig. 10(e), when 30 mL L⁻¹ of *t*-butanol was added to reaction system, OG oxidation was significantly suppressed with decolorization efficiency dropped from 100 to 33% at 60 min of treatment. This result confirmed the existence of $\cdot\text{OH}$ as primary reactive species in the plasma/laterite system. The results demonstrated that the addition of laterite to non-thermal gliding arc system could remarkably enhance decolorization of OG solution through a synergetic effect between non-thermal plasma treatment and heterogeneous catalysis, giving rise to “plasma-(photo)catalysis combined process”. Accordingly, the mechanism of OG oxidation was proposed in the following section.

3.5. Plasma-(photo)catalysis plausible mechanism

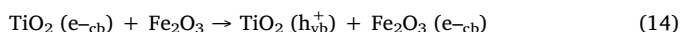
The high efficiency of OG oxidation is related to the combination of plasma treatment with laterite catalytic and photocatalytic activities. First of all, in humid air plasma gliding arc, the determining oxidizing species generated is hydroxyl radical ($\cdot\text{OH}$) via electron attacking water molecule (Eq. (70)) and /or by H₂O₂ photolysis (Eq. (8)).



Moreover, electrical discharge in water emitted UV-light (430 ≥ λ ≥ 190 nm) is sufficient for photochemical activation of semiconductor catalysts [14]. Under UV light irradiation, the following mechanism is proposed for TiO₂ photocatalysis in the presence of H₂O₂ to form active oxygen species.



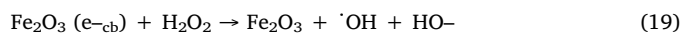
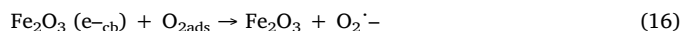
However, the Fe₂O₃ photocatalyst acted as TiO₂ sensitizer due to its narrow band-gap. Therefore, photo-generated electrons in TiO₂ valence band can be transferred into Fe₂O₃ conduction band (Eq. (14)).



The photogenerated holes in TiO₂ valence band reacted with adsorbed water molecules to form $\cdot\text{OH}$ (Eq. (15)).



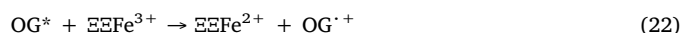
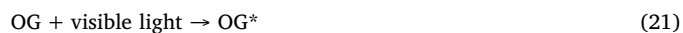
While, the electron transfer to Fe₂O₃ conduction band would react with dissolved molecular oxygen to generate a series of highly reactive species (Eqs. (16)–(19)).



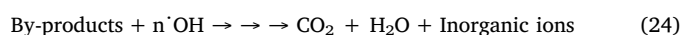
In addition, an integrated electric field in the Fe₂O₃-TiO₂ heterojunction favoured electron-holes charges separation by transferring electrons from TiO₂ conduction band to Fe₂O₃ [29]. Moreover, under experimental pH = 3 conditions, the positive charge of boehmite (pH_{pzc} = 7.5) enhanced the movement of the electrons from Fe₂O₃ by electrostatic attraction and hence depressed the recombination reaction of electron/hole pairs over TiO₂. The charge separation improved the lifetime of electrons which can reduce Fe³⁺ to Fe²⁺ on the surface of catalyst (Eq. (20)). The leaching test was performed in the solutions after the treatment and the determined soluble ion amount was less than 0.2% of total ion content. Therefore, this negligible amount of iron ion cannot display a significant contribution in OG oxidation through homogeneous Fenton based process. Despite the low concentration of leached iron ion (0.02 mM), heterogeneous Fenton-like processes can take place mediated by the surface attached Fe³⁺ ion (Eq. (21)).



Furthermore, under visible light irradiation, excited state dye can also reduce surface Fe³⁺ to Fe²⁺ through intermolecular electron transfer (Eqs. (21)–(22)), giving rise to dye-sensitized photo-Fenton reaction [50,51]:



Among the generated reactive species, $\cdot\text{OH}$ is the most efficient for organic pollutant degradation, owing to its high oxidation potential (2.8 V/SHE). In addition, to study the function of $\cdot\text{OH}$ during the plasma-(photo)catalytically combined process, *t*-butanol (30 mL L⁻¹) was added to the OG laterite suspension solution. From this experiment, the resulting decolorization efficiency as a function of treatment time is reported in Fig. 10(e). From this figure, it should be highlighted that, the decrease in OG decolorization efficiency compared to without *t*-butanol, represented a significant contribution of $\cdot\text{OH}$ in the combined process. Hence, OG molecule was oxidized by $\cdot\text{OH}$ until its mineralisation into CO₂, H₂O and inorganic ions (Eqs. (23) and (24)).



Based on the above discussion a plausible reaction pathway for $\cdot\text{OH}$ production and OG oxidation in presence of the laterite by heterogeneous (photo)catalytically assisted gliding arc plasma discharge was proposed in Fig. 11.

4. Conclusion

This study reported on OG oxidation in aqueous solution using Cameroonian natural laterite soil as the catalyst in combination of gliding arc non-thermal plasma treatment. The laterite calcined at

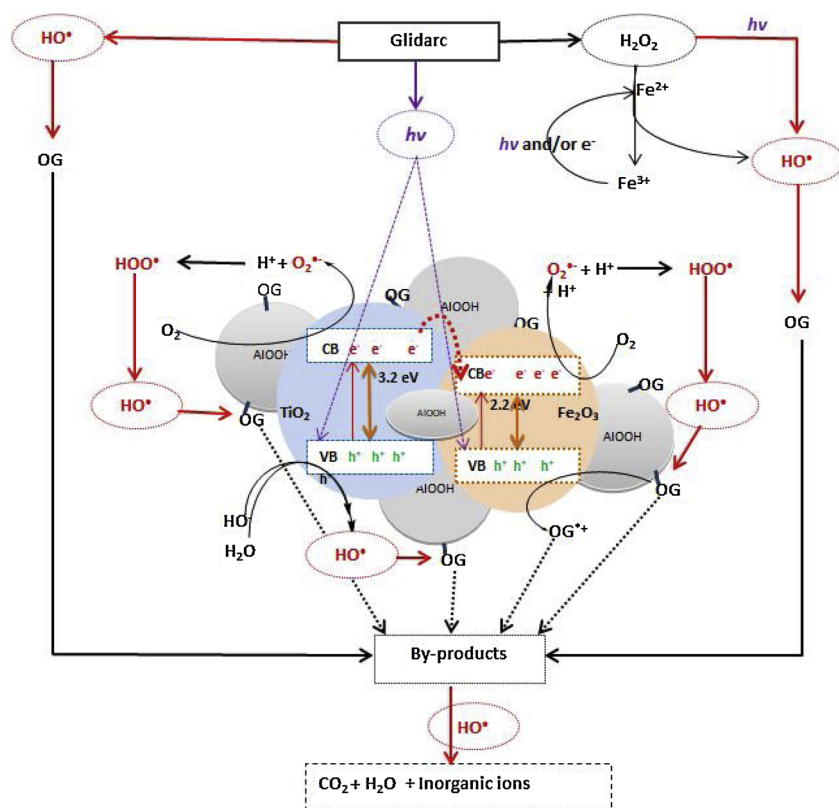


Fig. 11. Schematic representation of $\cdot\text{OH}$ production and degradation pathway for OG oxidation by $\cdot\text{OH}$ with laterite-mediated plasma-photocatalysis process.

400 °C exhibited good adsorption of OG dye owing to its high specific surface area and through numerous active Lewis sites present at boehmite surface. It was demonstrated that, incorporation of laterite into the gliding arc plasma treatment of OG aqueous solution remarkably improved the decolorization until the high mineralization yield. The following synergistic mechanisms could assist in achieving the high oxidation efficiency for OG oxidative degradation: (i) $\cdot\text{OH}$ production plasmachemical process and plasma-generated H_2O_2 photolysis, (ii) semiconductors TiO_2 photocatalysis generated excites electron-hole carriers which were reacted with H_2O molecules to form $\cdot\text{OH}$, (iii) photo-Fenton like process due to Fe^{3+} reaction with H_2O_2 in presence of plasma emitted UV light. Moreover, the laterite was not only an efficient catalyst for OG oxidation under non-thermal plasma condition but also a relative stable catalyst. With an increasing interest in a global market of heterogeneous catalyst and/or photocatalysts for wastewater treatment, the laterite, available in several regions of the world, can constitute a low cost and environmentally sustainable catalyst.

Acknowledgments

The authors are grateful to “Service de la Cooperation et d’Action Culturelle” (SCAC) of the Cameroon French Embassy for financial support. We are also grateful to “Centre de Recherches Petrographiques et Geochimiques” CRPG-Nancy for chemical composition analysis of laterite.

References

- [1] P.J. Bruggeman, M.J. Kushner, B.R. Locke, Plasma-liquid interactions: a review and roadmap, *Plasma Sources Sci. Technol.* 25 (2016) 053002.
- [2] B. Jiang, J. Zheng, S. Qiu, M. Wu, Q. Zhang, Z. Yan, Q. Xue, Review on electrical discharge plasma technology for wastewater remediation, *Chem. Eng. J.* 236 (2014) 348–368.
- [3] C.M. Du, J.H. Yan, B.G. Cheron, Degradation of 4-chlorophenol using a gas-liquid gliding arc discharge plasma reactor, *Plasma Chem. Plasma Process* 27 (2007) 635–646.
- [4] R. Burlica, M.J. Kirkpatrick, B.R. Locke, Formation of reactive species in gliding arc discharges with liquid water, *J. Electrostat.* 64 (2006) 35–43.
- [5] R. Burlica, K.Y. Shih, B.R. Locke, Formation of H_2 and H_2O_2 in a water-spray gliding arc nonthermal plasma reactor, *Ind. Eng. Chem. Res.* 49 (2010) 6342–6349.
- [6] C.M. Du, J.H. Yan, B. Cheron, Decomposition of toluene in a gliding arc discharge plasma reactor, *Plasma Sources Sci. Technol.* 16 (2007) 791–797.
- [7] M. Cheng, G. Zeng, D. Huang, C. Lai, P. Xu, C. Zhang, Y. Liu, Hydroxyl radicals based advanced oxidation processes (AOPs) for remediation of soils contaminated with organic compounds: a review, *Chem. Eng. J.* 284 (2016) 582–598.
- [8] Z. Wang, W. Ma, C. Chen, J. Zhao, Light-assisted decomposition of dyes over iron-bearing soil clays in the presence of H_2O_2 , *J. Hazard. Mater.* 168 (2009) 1246–1252.
- [9] J. Wang, Y. Sun, H. Jiang, J. Feng, Removal of caffeine from water by combining dielectric barrier discharge (DBD) plasma with goethite, *J. Saudi Chem. Soc.* (2016).
- [10] Y. Zhang, M. Zhou, L. Lei, Degradation of 4-chlorophenol in different gas-liquid electrical discharge reactors, *Chem. Eng. J.* 132 (2007) 325–333.
- [11] D.M. Willberg, P.S. Lang, R.H. Höchemer, A. Kratel, M.R. Hoffmann, Degradation of 4-chlorophenol, 3, 4-dichloroaniline, and 2, 4, 6-trinitrotoluene in an electro-hydraulic discharge reactor, *Environ. Sci. Technol.* 30 (1996) 2526–2534.
- [12] J.W. Robinson, M. Ham, A.N. Balaster, Ultraviolet radiation from electrical discharges in water, *J. Appl. Phys.* 44 (1973) 72–75.
- [13] C. Subrahmanyam, M. Magureanu, D. Laub, A. Renken, L. Kiwi-Minsker, Nonthermal plasma abatement of trichloroethylene enhanced by photocatalysis, *J. Phys. Chem. C* 111 (2007) 4315–4318.
- [14] A.M. Anpilov, E.M. Barkhudarov, Y.B. Bark, Y.V. Zadiraka, M. Christofi, Y.N. Kozlov, I.A. Kossyi, V.A. Kop'ev, V.P. Silakov, M.I. Taktakishvili, S.M. Temchin, Electric discharge in water as a source of UV radiation, ozone and hydrogen peroxide, *J. Phys. D Appl. Phys.* 34 (2001) 993–999.
- [15] J. Zhu, Z. Sun, Z. Li, A. Ehn, M. Alden, M. Salewski, F. Leipold, Y. Kusano, Dynamics OH distributions and UV emission of a gliding arc at various flow-rates investigated by optical measurements, *J. Phys. D Appl. Phys.* 47 (2014) 295203.
- [16] M. Gharagozian, D. Dorrnanian, Water treatment by the AC gliding arc air plasma, *J. Theor. Appl. Phys.* 11 (2017) 171–180.
- [17] E. Acayanka, D.S. Kuete, G.Y. Kamgang, S. Nzali, S. Laminsi, P.T. Ndifon, Synthesis, characterization and photocatalytic application of $\text{TiO}_2/\text{SnO}_2$ nanocomposite obtained under non-thermal plasma condition at atmospheric pressure, *Plasma Chem. Plasma Process* 36 (2016) 799–811.
- [18] A. Tiya-Djowe, E. Acayanka, G. Lontio-Nkoungof, S. Laminsi, E.M. Gaigneaux, Enhanced discoloration of methyl violet 10B in a gliding arc plasma reactor by the maghemite nanoparticles used as heterogeneous catalyst, *J. Environ. Chem. Eng.* 3 (2015) 953–960.
- [19] E. Acayanka, Tiya Djowe, S. Laminsi, C.C. Tchoumkwe, S. Nzali, A.P. Mbouopda,

- P.T. Ndifon, E.M. Gaigneaux, Plasma-assisted synthesis of TiO₂ nanorods by gliding arc discharge processing at atmospheric pressure for photocatalytic applications, *Plasma Chem, Plasma Process.* 33 (2013) 725–735.
- [20] M.R. Ghezzer, F. Abdelmalek, M. Belhadj, N. Benderdouche, A. Addou, Gliding arc plasma assisted photocatalytic degradation of anthraquinonic acid green 25 in solution with TiO₂, *Appl. Catal. B: Environ.* 72 (2007) 304–313.
- [21] C.S. Turchi, D.F. Ollis, Photocatalytic degradation of organic water contaminants: mechanisms involving hydroxyl radical attack, *J. Catal.* 122 (1990) 178–192.
- [22] B. Jiang, Y. Gong, J. Gao, T. Sun, Y. Liu, N. Oturan, M.A. Oturan, The reduction of Cr(VI) to Cr(III) mediated by environmentally relevant carboxylic acids: state-of-the-art and perspectives, *J. Hazard. Mater.* 365 (2019) 205–226.
- [23] L. Duan, N. Jiang, N. Lu, K. Shang, J. Li, Y. Wu, Synergetic effect of TiO₂ and Fe³⁺ as co-catalysts for enhanced phenol degradation in pulsed discharge system, *Appl. Catal. B: Environ.* 221 (2018) 521–529.
- [24] M. Kamagate, A.A. Assadi, T. Kone, S. Giraudet, L. Coulibaly, K. Hanna, Use of laterite as a sustainable catalyst for removal of fluoroquinolone antibiotics from contaminated water, *Chemosphere* 195 (2018) 847–853.
- [25] C.O. Swanson, The origin, distribution and composition of laterite, *J. Am. Ceram. Soc.* 6 (1923) 1248–1260.
- [26] A.R. Khataee, S.G. Pakdehi, Removal of sodium azide from aqueous solution by Fenton-like process using natural laterite as a heterogeneous catalyst: kinetic modeling based on nonlinear regression analysis, *J. Taiwan Inst. Chem. Eng.* 45 (2014) 2664–2672.
- [27] A. Czernichowski, Glidarc assisted preparation of the synthesis gas from natural and waste hydrocarbons gases, *Oil Gas Sci. Technol.* 56 (2001) 181–198.
- [28] G. Mendoza-Damián, F. Tzompantzi, R. Pérez-Hernández, R. Gómez, A. Hernández-Gordillo, Photocatalytic properties of boehmite-SnO₂ composites for the degradation of phenol, *Catal. Today* 266 (2016) 82–89.
- [29] P. Xu, G.M. Zeng, D.L. Huang, C.L. Feng, S. Hu, M.H. Zhao, C. Lai, Z. Wei, C. Huang, G.X. Xie, Z.F. Liu, Use of iron oxide nanomaterials in wastewater treatment: a review, *Sci. Total Environ.* 424 (2012) 1–10.
- [30] H. Al-Sheeha, M. Marafi, A. Stanislaus, Reclamation of alumina as boehmite from an alumina-supported spent catalyst, *Int. J. Miner. Process.* 88 (2008) 59–64.
- [31] M. Hanesch, Raman spectroscopy of iron oxides and (oxy)hydroxides at low laser power and possible applications in environmental magnetic studies, *Geophys. J. Int.* 177 (2009) 941–948.
- [32] S.K. Gupta, R. Desai, P.K. Jha, S. Sahoo, D. Kirin, Titanium dioxide synthesized using titanium chloride: size effect study using Raman spectroscopy and photoluminescence, *J. Raman Spectrosc.* 41 (2010) 350–355.
- [33] H. Cheng, J. Yang, Q. Liu, J. Zhang, R.L. Frost, A spectroscopic comparison of selected Chinese kaolinite, coal bearing kaolinite and halloysite - A mid-infrared and near-infrared study, *Spectrochim. Acta - Part A Mol. Biomol. Spectrosc.* 77 (2010) 856–861.
- [34] E. Balan, M. Lazzeri, G. Morin, F. Mauri, First-principles study of the OH-stretching modes of gibbsite, *Am. Mineral.* 91 (2006) 115–119.
- [35] C. Ruales-Lonfat, J.F. Barona, A. Sienkiewicz, M. Bensimon, J. Vélez-Colmenares, N. Benítez, C. Pulgarín, Iron oxides semiconductors are efficient for solar water disinfection: a comparison with photo-Fenton processes at neutral pH, *Appl. Catal. B: Environ.* 166–167 (2015) 497–508.
- [36] T. Zhang, C. Li, J. Ma, H. Tian, Z. Qiang, Surface hydroxyl groups of synthetic α -FeOOH in promoting [•]OH generation from aqueous ozone: property and activity relationship, *Appl. Catal. B: Environ.* 82 (2008) 131–137.
- [37] H.D. Ruan, R.L. Frost, J.T. Klopogge, L. Duong, Infrared spectroscopy of goethite dehydroxylation: III. FT-IR microscopy of in situ study of the thermal transformation of goethite to hematite, *Spectrochim. Acta - A Mol. Biomol. Spectrosc.* 58 (2002) 967–981.
- [38] J.T. Klopogge, H.D. Ruan, R.L. Frost, Thermal decomposition of bauxite minerals: infrared emission spectroscopy of gibbsite, boehmite and diaspore, *J. Mater. Sci.* 37 (2002) 1121–1129.
- [39] O.S.N. Sum, J. Feng, X. Hu, P.L. Yue, Photo-assisted fenton mineralization of an azo-dye acid black 1 using a modified laponite clay-based Fe nanocomposite as a heterogeneous catalyst, *Top. Catal.* 33 (2005) 233–242.
- [40] D. Rahul Reddy, G. Kumaravel Dinesh, S. Anandan, Thirugnanasambandam Sivasankar, Sonophotocatalytic treatment of Naphthol Blue Black dye and real textile wastewater using synthesized Fe doped TiO₂, *Chem. Eng. Process.* 99 (2016) 10–18.
- [41] Z.R. Lin, L. Zhao, Y.H. Dong, Quantitative characterization of hydroxyl radical generation in a goethite-catalyzed Fenton-like reaction, *Chemosphere* 141 (2015) 7–12.
- [42] F.F. Dias, A.A.S. Oliveira, A.P. Arcanjo, F.C.C. Moura, J.G.A. Pacheco, Residue-based iron catalyst for the degradation of textile dye via heterogeneous photo-Fenton, *Appl. Catal. B: Environ.* 186 (2016) 136–142.
- [43] K. Hayat, M.A. Gondal, M.M. Khaled, S. Ahmed, A.M. Shamsi, Nano ZnO synthesis by modified sol gel method and its application in heterogeneous photocatalytic removal of phenol from water, *Appl. Catal. A Gen.* 393 (2011) 122–129.
- [44] D. Dvoranová, V. Brezová, M. Mazúr, M.A. Malati, Investigations of metal-doped titanium dioxide photocatalysts, *Appl. Catal. B: Environ.* 37 (2002) 91–105.
- [45] J. Sun, X. Wang, J. Sun, R. Sun, S. Sun, L. Qiao, Photocatalytic degradation and kinetics of Orange G using nano-sized Sn(IV)/TiO₂/AC photocatalyst, *J. Mol. Catal. A Chem.* 260 (2006) 241–246.
- [46] T. Echigo, D.M. Aruguete, M. Murayama, M.F. Hochella, Influence of size, morphology, surface structure, and aggregation state on reductive dissolution of hematite nanoparticles with ascorbic acid, *Geochim. Cosmochim. Acta* 90 (2012) 149–162.
- [47] Z. Li, J. Sheng, Y. Wang, Y. Xu, Enhanced photocatalytic activity and stability of alumina supported hematite for azo-dye degradation in aerated aqueous suspension, *J. Hazard. Mater.* 254–255 (2013) 18–25.
- [48] X. Zhang, M. Honkanen, E. Levänen, T. Mäntylä, Transition alumina nanoparticles and nanorods from boehmite nanoflakes, *J. Cryst. Growth* 310 (2008) 3674–3679.
- [49] A.V. Emeline, G.V. Kataeva, V.K. Ryabchuk, N. Serpone, Photostimulated generation of defects and surface reactions on a series of wide band gap metal-oxide solids, *J. Phys. Chem. B* 103 (1999) 9190–9199.
- [50] M. Cheng, W. Song, W. Ma, C. Chen, J. Zhao, J. Lin, H. Zhu, Catalytic activity of iron species in layered clays for photodegradation of organic dyes under visible irradiation, *Appl. Catal. B: Environ.* 77 (2008) 355–363.
- [51] R. Liu, D. Xiao, Y. Guo, Z. Wang, J. Liu, A novel photosensitized Fenton reaction catalyzed by sandwiched iron in synthetic nontronite, *RSC Adv.* 4 (2014) 12958–12963.